Eur. Phys. J. B (2018) 91: 99
https://doi.org/10.1140/epjb/e2018-90165-x

THE EUROPEAN PHYSICAL JOURNAL B

Regular Article

A screened independent atom model for the description of ion collisions from atomic and molecular clusters*

Hans Jürgen Lüdde[1], Marko Horbatsch[2,a], and Tom Kirchner[2]

[1] Institut für Theoretische Physik, Goethe-Universität, 60438 Frankfurt, Germany
[2] Department of Physics and Astronomy, York University, Toronto, Ontario M3J 1P3, Canada

Received 13 March 2018 / Received in final form 9 April 2018
Published online 4 June 2018 – © EDP Sciences, Società Italiana di Fisica, Springer-Verlag 2018

Abstract. We apply a recently introduced model for an independent-atom-like calculation of ion-impact electron transfer and ionization cross sections to proton collisions from water, neon, and carbon clusters. The model is based on a geometrical interpretation of the cluster cross section as an effective area composed of overlapping circular disks that are representative of the atomic contributions. The latter are calculated using a time-dependent density-functional-theory-based single-particle description with accurate exchange-only ground-state potentials. We find that the net capture and ionization cross sections in p-X_n collisions are proportional to n^α with $2/3 \leq \alpha \leq 1$. For capture from water clusters at 100 keV impact energy α is close to one, which is substantially different from the value $\alpha = 2/3$ predicted by a previous theoretical work based on the simplest-level electron nuclear dynamics method. For ionization at 100 keV and for capture at lower energies we find smaller α values than for capture at 100 keV. This can be understood by considering the magnitude of the atomic cross sections and the resulting overlaps of the circular disks that make up the cluster cross section in our model. Results for neon and carbon clusters confirm these trends. Simple parametrizations are found which fit the cross sections remarkably well and suggest that they depend on the relevant bond lengths.

1 Introduction

Ionization in charged-particle matter interactions is a process of relevance to both fundamental and more applied research areas, but is difficult to describe in quantitative terms if the objects under study are sufficiently complex. On the experimental side, challenges associated with preparation and control of the projectile and target species as well as the detection of multiple reaction products, possibly in coincidence, have to be addressed. On the theoretical side, the challenge resides in the description of an interacting few- or many-body system far away from its ground state, a problem that is straightforward to formulate for (nonrelativistic) Coulomb systems, but hard to solve even with present-day supercomputers [1].

Time-dependent density functional theory (TDDFT) was conceived by Runge and Gross [2] with this problem in mind and the objective to develop a time-dependent description of scattering experiments that would circumvent the calculation of the many-body wave function [3]. However, applications of the time-dependent Kohn-Sham (TDKS) scheme to collision problems have remained relatively sparse. This is different from the situation for the somewhat related problem of ionization in strong laser fields (see, e.g., the books [4,5] and references therein). There are no obvious symmetries in collisional ionization and furthermore for positively charged projectile ions direct target ionization competes with electron transfer to bound projectile states. In the framework of the semiclassical approximation, in which the projectile is assumed to move on a classical (straight-line) path, projectile-centered states must be augmented by so-called electron translation factors (ETFs) to account for the relative motion and preserve Galilean invariance.

These issues have been analyzed in some detail for the two-center ion-atom case, often for prototypical one-electron problems such as the proton-hydrogen collision system [6,7]. Collisions involving helium are perhaps the next best studied systems, but the vast majority of calculations have been based on simplified descriptions since explicit solutions of the two-electron time-dependent Schrödinger equation are exceedingly difficult and computationally costly (see, e.g., Ref. [8] and references therein). For atoms with more than two electrons, let alone for the atomic and molecular clusters addressed in the present work, they are out of reach.

A popular framework for a simplified treatment of many-electron collision systems is the independent electron model (IEM). However, the most sophisticated IEM variant, the time-dependent Hartree-Fock (TDHF) scheme, has been applied to only a handful of cases. This is due to difficulties associated with the nonlocal exchange interaction and, more fundamentally, with the nonlinearity of the TDHF equations, which manifests itself

* Contribution to the Topical Issue "Special issue in honor of Hardy Gross", edited by C.A. Ullrich, F.M.S. Nogueira, A. Rubio, and M.A.L. Marques.

[a] e-mail: marko@yorku.ca

in the occurrence of fluctuating transition probabilities when analyzing the TDHF wave function with respect to eigenstates of a static asymptotic Hamiltonian [9–11]. The latter problem is known as the TDHF cross channel correlation or projection problem and has also been discussed in the context of nuclear reactions [12,13].

About 20 years ago we started to look into atomic collisions involving many-electron targets such as neon and argon atoms using a TDDFT-inspired single-particle description based on atomic ground-state DFT potentials [14,15]. The time dependence of these potentials over the course of the collision was neglected and the projection problem avoided. Orbital propagation was achieved using the basis generator method (BGM), a basis set expansion technique built on atomic orbitals and dynamically adapted pseudostates [16]. The BGM and the more recent two-center version TC-BGM [17] proved capable of accounting for target excitation, electron transfer, and ionization channels in ion-atom collision problems over a wide range of collision energies (see, e.g., Refs. [18,19] and references therein).

Subsequently, we amended the no-response approximation of frozen ground-state potentials by simple response models which did not increase the computational burden significantly and allowed us to analyze the projection problem and study dynamical potential effects in a semi-quantitative way [20]. We found that response has the tendency to lower probabilities for total electron removal (the sum of electron transfer to the projectile and direct target ionization) at low to intermediate collision energies. As soon as the projectile speed is significantly larger than the average orbital velocity of a given target electron, that electron becomes insensitive to time-dependent changes in the interelectronic potential simply because ionization happens too rapidly. As a consequence, response model cross sections approach no-response results towards high collision energies. Also, response effects turned out ot be generally small for proton impact on first-row elements. This is so because multiple-electron removal is a weak process in these collisions and our model is designed in such a way that dynamical screening becomes appreciable only after one electron is removed on average. This choice was motivated by the success of so-called frozen TDHF calculations in studies concerned with the (photo-) ionization of a single electron [21].

Collisions of projectile ions (with or without projectile electrons) from small molecules, such as H_2O [22,23], or CH_4 [24] were treated within a framework where simple self-consistent field wave functions were projected onto atomic orbitals calculated in DFT. These orbitals were then evolved using the TC-BGM, and transition amplitudes were calculated on the basis of interpreting Kohn-Sham determinants. For biomolecules and clusters this approach is not suitable. Direct implementations of TDDFT equations for ion collisions with small molecules were reported by other groups [25,26]. For larger systems a few calculations based on first-principles approaches have been carried out [27–29], but most of the available cross section results for electron transfer and target ionization have been obtained using simplified and classical models (see, e.g., Refs. [30–34] and references therein).

Given this situation we recently introduced an independent-atom-model (IAM) description to deal with complex multicenter collision systems on the basis of atomic no-response TC-BGM calculations [35]. The simplest realization of the IAM is Bragg's additivity rule (IAM-AR) according to which a net cross section for a complex target such as a molecule or cluster is obtained from adding up atomic net cross sections for all atoms that make up the system. Our model goes beyond the IAM-AR by associating the atomic cross sections in the AR sum with weight factors. The latter are determined from a geometrical interpretation of a cross section as an effective area using the following procedure. First, each atom in a given target is surrounded by a sphere of a radius representative of the atomic cross section for either net electron transfer to the projectile or to the continuum (for brevity referred to as net capture and net ionization in the following). Secondly, the resulting three-dimensional structure of overlapping spheres is projected on a plane which is perpendicular to the projectile beam axis. In the last step, the effective area in that plane is taken as the cross section for net capture or net ionization of the system in that particular geometry. An orientation average is calculated to make contact with experimental data for randomly oriented molecules or clusters. We refer to the model as IAM-PCM, since the effective cross-sectional area, and by extension the weight factors attached to the atomic contributions in a given orientation, are calculated using a pixel counting method (PCM).

The IAM-PCM was successfully applied to a number of collision systems involving proton projectiles and molecular targets such as CO, H_2O, and $C_4H_4N_2O_2$ (uracil). It was demonstrated that IAM-AR cross sections for net capture and ionization are reduced substantially and agreement with experimental data is improved in regions in which the atomic cross section contributions are large and the overlap effects significant [35].

In this work, we use the IAM-PCM to calculate net capture and ionization cross sections in proton collisions with water, neon, and carbon clusters comprising systems with hydrogen bonds, van der Waals bonds, and covalent bonds. We begin in Section 2 with a discussion of the atomic ingredients, i.e., the solution of the (approximate) ion-atom TDKS equations using the TC-BGM (Sect. 2.1), the calculation of cross sections for net capture and ionization (Sect. 2.2), and results for the p-H, p-C, p-O, and p-Ne systems (Sect. 2.3). This is followed by a description of the IAM-PCM in Section 3. Results for the proton-cluster collision systems are presented in Section 4, and the paper ends with a few concluding remarks in Section 5. Atomic units, characterized by $\hbar = m_e = e = 4\pi\epsilon_0 = 1$, are used unless otherwise stated.

2 The basis generator method for ion-atom collisions

2.1 Solution of the single-particle equations

The TDKS scheme was anticipated by Runge and Gross in their original 1984 work [2] and put on firm grounds

by van Leeuwen in 1999 [36]. For a thorough discussion of the foundational theorems of TDDFT we refer the reader to the books [4,5] and references therein.

For an N-electron ion-atom collision problem in the semiclassical approximation the TDKS equations can be written in the form

$$i\partial_t\psi_i(\mathbf{r},t) = \left(-\frac{1}{2}\nabla^2 - \frac{Z_T}{r_T} - \frac{Z_P}{r_P} + v_{ee}[n](\mathbf{r},t)\right)\psi_i(\mathbf{r},t), \quad i = 1,\ldots,N, \tag{1}$$

where $\mathbf{r}$, $\mathbf{r}_T$, and $\mathbf{r}_P$ denote the electronic position vector with respect to the center of mass (CM), the target, and the projectile, respectively, and Z_T and Z_P are the charge numbers of the nuclei. We assume the projectile to follow a straight-line path $\mathbf{R}(t) = \mathbf{r}_T - \mathbf{r}_P = (b, 0, vt)$ characterized by the impact parameter b and the constant speed v.

The effective electron-electron potential v_{ee} in equation (1) is a functional of the density n and can be split into the usual Hartree, exchange, and correlation contributions. In the no-response approximation for the problem of a bare projectile ion impinging on an atomic target, v_{ee} is given by a (spherically-symmetric) ground-state DFT potential. More specifically, we use Hartree-exchange potentials obtained from the exchange-only version of the optimized potential method (OPM) [37,38] for the neutral ($N = Z_T$) carbon, oxygen, and neon atoms of interest in the present study and neglect correlation effects. An important feature of the OPM potentials is their complete cancellation of self-interaction contributions contained in the Hartree potential such that the correct asymptotic behaviour

$$v_{ee}^{\mathrm{OPM}}(r_T) \overset{r_T\to\infty}{\to} \frac{N-1}{r_T} \tag{2}$$

is ensured. This is crucial for a proper description of target electron removal [14,15].

The approximate TDKS equations (1) with the ground-state potential v_{ee}^{OPM} are propagated using the TC-BGM, which, like any basis-expansion technique, assumes that the solutions can be represented in terms of a finite set of states. The TC-BGM set includes N_T atomic states on the target center, i.e., bound eigenstates of

$$\hat{h}_T = -\frac{1}{2}\nabla^2 - \frac{Z_T}{r_T} + v_{ee}^{\mathrm{OPM}}(r_T) \tag{3}$$

$$\equiv -\frac{1}{2}\nabla^2 + V_T, \tag{4}$$

a set of N_P eigenstates of the projectile Hamiltonian

$$\hat{h}_P = -\frac{1}{2}\nabla^2 - \frac{Z_P}{r_P} \equiv -\frac{1}{2}\nabla^2 + V_P \tag{5}$$

to describe capture, and a set of pseudostates which overlap with the continuum. It is the specific choice of the latter that distinguishes the TC-BGM from other coupled-channel methods for atomic collisions. The guiding idea is to span a subspace of Hilbert space which dynamically adapts to the time evolution of the system in such a way that couplings to the complementary space are small and can be neglected without introducing significant errors. The benefit of using time-dependent basis states is that one can hope for reasonable convergence without having to include a very large number of states.

It was shown on theoretical grounds [16] and demonstrated in a number of practical applications (see, e.g., Refs. [18,19] and references therein) that good convergence can be achieved by using basis functions of the form

$$\chi_j^J(\mathbf{r},t) = [W_P(r_P)]^J \phi_j^0(\mathbf{r},t) \tag{6}$$

$$W_P(r_P) = \frac{1}{r_P}\left(1 - \mathrm{e}^{-r_P}\right) \tag{7}$$

$$\phi_j^0(\mathbf{r},t) = \begin{cases} \phi_j(\mathbf{r}_T)\exp(i\mathbf{v}_T\cdot\mathbf{r}) \text{ if } j \le N_T \\ \phi_j(\mathbf{r}_P)\exp(i\mathbf{v}_P\cdot\mathbf{r}) \text{ if } N_T < j \le N_T + N_P, \end{cases} \tag{8}$$

where $\mathbf{v}_T$ and $\mathbf{v}_P$ denote the (constant) velocities of the target and projectile with respect to the CM, and the functions ϕ_j on the right hand side of equation (8) satisfy stationary eigenvalue equations for $\hat{h}_T$ ($j \le N_T$) and $\hat{h}_P$ ($j > N_T$) in the (moving) target and projectile reference frames, respectively. The phase factors are ETFs which ensure Galilean invariance. Acting with spatial and time derivative operators on them leads to the modified eigenvalue equations

$$(\hat{h}_{T,P} - i\partial_t)|\phi_j^0\rangle = g_j|\phi_j^0\rangle \tag{9}$$

with

$$g_j = \varepsilon_j + \frac{v_{T,P}^2}{2} \tag{10}$$

and atomic energy eigenvalues ε_j for the target and projectile orbitals $\phi_j^0(\mathbf{r},t) = \langle\mathbf{r}|\phi_j^0\rangle$ in the CM reference frame.

Expanding the TDKS orbitals in this non-orthogonal, time-dependent TC-BGM basis

$$\psi_i(\mathbf{r},t) = \sum_{j,J} c_{j,J}^i(t)\chi_j^J(\mathbf{r},t) \tag{11}$$

turns the single-particle equations into a set of coupled equations for the expansion coefficients

$$i\sum_{j,J} S_{kj}^{KJ}(t)\dot{c}_{j,J}^i(t) = \sum_{j,J} M_{kj}^{KJ}(t)c_{j,J}^i(t) \tag{12}$$

with overlap

$$S_{kj}^{KJ} = \langle kK|jJ\rangle \tag{13}$$

and interaction

$$M_{kj}^{KJ} = \langle kK|\hat{h}_T + V_P - i\partial_t|jJ\rangle \tag{14}$$

matrix elements. In equations (13) and (14) we have used the short-hand notation

$$|jJ\rangle = W_P^J |j0\rangle \tag{15}$$

for the BGM basis states, i.e., the functions $\chi_j^J(\mathbf{r},t) = \langle \mathbf{r}|jJ\rangle$.

The calculation of the matrix elements proceeds in several steps. First, the interaction matrix elements (14), are rewritten by using similar arguments as in references [39] and [23] to arrive at

$$M_{kj}^{KJ} = \langle kK|\frac{KJ}{2}\left(\frac{\nabla W_P}{W_P}\right)^2 + \frac{K}{K+J}V_{\bar{j}} + \frac{J}{K+J}V_{\bar{k}}|jJ\rangle - \frac{J}{K+J}i\partial_t\langle kK|jJ\rangle + \frac{Kg_j + Jg_k}{K+J}\langle kK|jJ\rangle, \tag{16}$$

where for $j \leq N_T$ we set $V_{\bar{j}} = V_P$ and $V_j = V_T$, while for $j > N_T$ we set $V_{\bar{j}} = V_T$ and $V_j = V_P$. In contrast to equation (14) the equivalent form (16) does not involve derivatives of basis functions.

In a second step, the set of TC-BGM pseudostates $\{|jJ\rangle, J > 0\}$ is orthogonalized to the generating two-center basis $\{|j0\rangle\}$ to separate the ionized and bound parts of the TDKS orbitals. Finally, an LU decomposition is carried out to turn the basis into a completely orthonomalized set of states and the coupled-channel equations (12) into the form

$$i\dot{\mathbf{d}}^i = \tilde{\mathsf{M}}\mathbf{d}^i, \tag{17}$$

in which $\tilde{\mathsf{M}}$ is the transformed interaction matrix and $\mathbf{d}^i$ the transformed expansion coefficient vector of the i-th TDKS orbital. The set of matrix equations (17) is solved using standard methods [40].

2.2 Calculation of net cross sections

The atomic contributions used in the IAM-AR and IAM-PCM are cross sections for net capture and net ionization. They are calculated, exploiting cylindrical symmetry, via

$$\sigma^{\text{net }x} = 2\pi\int_0^\infty bP^{\text{net }x}(b)db, \tag{18}$$

where x denotes capture (x = cap) or ionization (x = ion) and $P^{\text{net }x}$ is the corresponding (impact-parameter-dependent) net electron number. Provided that at an asymptotic time t_f after the collision the one-particle density n can be split into non-overlapping contributions associated with electrons captured by the projectile (P), promoted to the continuum (C) and retained by the target (T), one can write for the total electron number [41]

$$N = \int_P n(\mathbf{r},t_f)d^3r + \int_C n(\mathbf{r},t_f)d^3r + \int_T n(\mathbf{r},t_f)d^3r, \tag{19}$$

where the integrals are over (non-overlapping) P, C, and T subspaces, and identify

$$P^{\text{net cap}} = \int_P n(\mathbf{r},t_f)d^3r, \tag{20}$$

$$P^{\text{net ion}} = \int_C n(\mathbf{r},t_f)d^3r. \tag{21}$$

Equations (20) and (21) show that net electron numbers, and as a consequence of equation (18) net cross sections as well, are explicit density functionals. This makes them convenient observables in TDDFT-based studies: The only fundamental approximation involved in a TDDFT net cross section calculation is the choice made for the TDKS potential. If one wishes to calculate a cross section that corresponds to a coincident measurement of single or multiple capture and ionization, one faces the additional challenge that the exact density dependence of the observables is not known and additional approximations are required [8,41].

We conclude this section by noting that instead of integrating the electron density over subspaces of $\mathcal{R}^3$ we use the TC-BGM basis representation to calculate net capture and ionization directly from the asymptotic expansion coeffients of equation (17)

$$P^{\text{net cap}} = \sum_{i=1}^{N}\sum_{k}^{P}|d_k^i(t_f)|^2, \tag{22}$$

$$P^{\text{net ion}} = N - P^{\text{net cap}} - \sum_{i=1}^{N}\sum_{k}^{T}|d_k^i(t_f)|^2. \tag{23}$$

If the sums over k include all appreciably populated bound projectile (P) and target (T) states and provided the above-mentioned condition of non-overlapping P, T, and C components is fulfilled, the channel and real-space representations of $P^{\text{net cap}}$ and $P^{\text{net ion}}$ are equivalent.

2.3 Sample results

In Figure 1 we show no-response TC-BGM net ionization and net capture cross section results for the proton-atom collision systems of interest in this work: p-H, p-C, p-O, and p-Ne. The p-H system in particular has been studied extensively over the years and many sets of theoretical results have been reported. Figure 1 does not provide comparisons with those previous calculations, since a review of the current status of atomic cross section calculations is outside the scope of this article. The purpose of Figure 1 is limited to an illustration of the level of accuracy and the asymptotic behaviour obtained in the (no-response) TC-BGM framework. To this end, experimental data for p-H and p-Ne, the only systems for which direct measurements of net ionization and capture cross sections are available, and fits of the asymptotic Bethe-Born ionization cross section formula [42,43]

$$\sigma_{\text{Bethe}} = \frac{A\ln E + B}{E}, \tag{24}$$

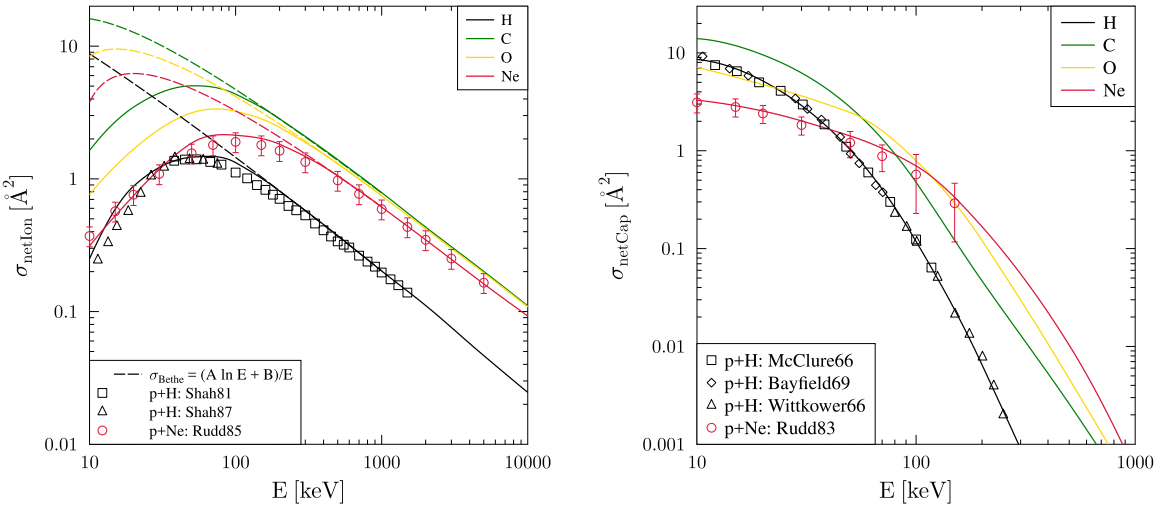

Fig. 1. Total cross sections for net ionization (left panel) and net capture (right panel) in p-H, p-C, p-O, and p-Ne collisions as functions of impact energy. Experiments: Shah81 [58], Shah87 [59], Rudd85 [60], McClure66 [61], Bayfield69 [62], Wittkower66 [63], Rudd83 [64]. For the p-H system the reported experimental uncertainties are below 10% and the error bars are smaller than the size of the symbols.

in which E is the projectile energy and A and B are treated as fit parameters, are included. For a broader discussion of p-H cross section results we refer the reader to the recent work [44]. The p-O and p-Ne systems were studied in our previous papers [45,46], respectively.

For the various atomic targets we included in the basis all atomic orbitals of the $KLMN$ shells of both projectile and target plus sets of 73–111 pseudostates constructed according to equations (6) and (7). The Bethe-Born cross sections were obtained by fitting the parameters A and B of equation (24) to the current TC-BGM results at high energies using the Fano representation, in which $E\sigma^{\rm net\,ion}$ is plotted against $\ln(E)$ (using appropriate units) [43]. For the p-H system the fitted parameters are consistent with the values that can be deduced from Bethe's original work [42].

Obviously, the agreement of the TC-BGM results with the experimental data and the Bethe-Born prediction at high E is very good. It is interesting to see that the net ionization cross sections for p-C and p-O do not only agree in shape, but also in magnitude in this region. For the oxygen case we found excellent agreement with experimental data for equivelocity electron impact corresponding to $E \geq$ 200 keV [45], which confirms the validity of first-order perturbation theory. Furthermore, within 10% accuracy the high-energy p-C and p-O results are four times larger than the p-H ionization cross section and, as found in additional calculations (not included in Fig. 1), they also coincide (within 10%) with results for p-N collisions. This implies that for a large class of biomolecules consisting of H, C, N, and O atoms the IAM-AR will predict very simple scaling relations. We found, somewhat surprisingly, that the same relations hold within the IAM-PCM described in the next section. An analysis of these scaling relations will be presented in a future publication focusing on ion-biomolecule collisions.

3 A pixel counting method for screened independent atom model calculations

The IAM-PCM is best explained by way of an example. Consider net capture in p-H_2O collisions at relatively low impact energy E. The ingredients of the IAM are the net capture cross sections for p-H and p-O collisions. These cross sections are assigned radii according to

$$r_j = [\sigma_j^{\rm net\,cap}/\pi]^{1/2}, \tag{25}$$

where $j = 1, 2, 3$ enumerates the atoms. We place the $L = 3$ atomic nuclei at their equilibrium positions in ground-state H_2O and surround each of them by a sphere of radius r_j. The impinging projectile then encounters an object made up of overlapping spheres and an effective cross-sectional area is determined by projecting that object on the plane that is perpendicular to the projectile beam.

Figure 2a displays the overlapping spheres for capture at $E = 10$ keV. It is important to keep in mind that the object shown is not a model of the water molecule, but a three-dimensional representation of net capture. A projectile approaching the molecule from a given direction will "see" the projected cross-sectional area as in classical scattering from superimposed hard spheres. Figure 2b shows this projection for projectile impact along the z-direction of the coordinate system used. The effective area, i.e., the molecular net cross section, can be represented as a weighted sum of atomic cross sections

$$\sigma_{\rm mol}^{{\rm net}\,x}(E,\alpha,\beta,\gamma) = \sum_{j=1}^{L} s_j^x(E,\alpha,\beta,\gamma)\sigma_j^{{\rm net}\,x}(E) \tag{26}$$

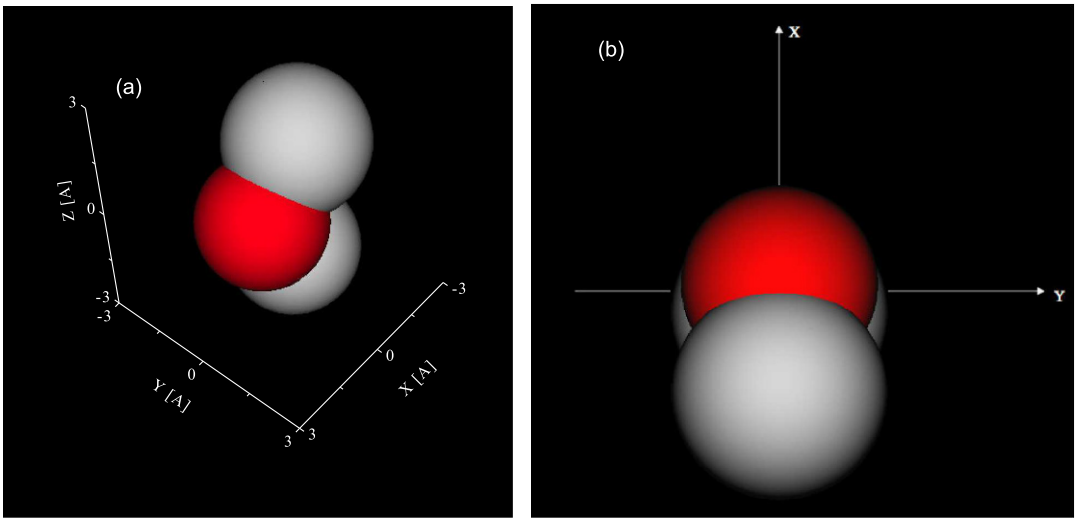

Fig. 2. Net capture in p-H_2O collisions at $E = 10$ keV: (a) three-dimensional image and (b) projection on the x-y plane. The radii of the spheres and circular disks are determined acoording to equation (25).

with weight factors $0 \leq s_j^x \leq 1$ and the Euler angles α, β, γ which characterize the orientation of the molecule. The notation used in equation (26) shows the dependencies of the various quantities and indicates that we use the prescription for both capture and ionization. We note in passing that the screening corrected additivity rule (SCAR) for electron-molecule scattering is based on similar ideas and uses a similar equation, but with orientation-independent weight factors that are obtained from a heuristic recurrence relation [47].

Figure 3 shows net capture at the higher energy $E = 100$ keV. At this energy, the atomic net capture cross sections are small and the spheres do not overlap. The projection on the x-y plane is simply the sum of the atomic cross sections, i.e., the weight factors are equal to one and the IAM-AR result is recovered.

In practice, we calculate the cross-sectional area of overlapping circular disks in the following way. The x–y plane is represented by a (pixel) matrix of dimension 1000×1000 with square elements (pixels) whose size is determined by choosing a resolution (we typically use $0.01\times$ 0.01 Å^2 pixels). The circular atomic cross section disks are "colored" according to their atomic identifier j and the pixel matrix is filled with the identifiers corresponding to the atomic cross sections from background to foreground as seen by the impinging projectile. For each j the area that is exposed to the projectile is determined by counting the visible pixels of that color and the screening coefficients in equation (26) are obtained by normalizing the area to the total (unscreened) atomic cross section

$$s_j^x(E, \alpha, \beta, \gamma) = \frac{\sigma_j^{\mathrm{vis}\,x}(E, \alpha, \beta, \gamma)}{\sigma_j^{\mathrm{net}\,x}(E)}. \qquad (27)$$

It was noted in reference [35] that the procedure can be criticized for overemphasizing the contribution of an atom located at the front, while possibly completely neglecting the contribution of an atom at the back of the molecule (cf. Fig. 2b). However, as long as one is interested in net cross sections only, this is a minor concern, since there is no need to attach physical significance to the individual screening coefficients and partial cross section areas. One may view them as purely auxiliary quantities to calculate the total projected area according to equation (26). Obviously, the area can be decomposed in different, but equivalent ways.

To make contact with experimental data for randomly oriented molecules, IAM-PCM calculations are carried out for a number of orientations and are averaged over the Euler angles. For all results shown in this work we exploit the fact that a rotation about the z-axis does not change the size of the visible area and vary only two out of three Euler angles on fine grids for a total of 40×40 orientations.

As an illustration, we consider the p-H_2O system in Figure 4. We compare IAM-PCM net capture and ionization cross sections with experimental data and with previous TC-BGM calculations obtained in the molecular framework mentioned in the Introduction, in which simple self-consistent field wave functions were projected onto atomic orbitals calculated in DFT [23].

For net ionization (Fig. 4a) the IAM-PCM outperforms the molecular TC-BGM: The cross section maximum appears at the correct position and the agreement with the measurements of Rudd and coworkers [48] is very good, except at energies below 20 keV where these data are underestimated. By contrast, the molecular TC-BGM cross section curve peaks at too low an energy and underestimates the experimental data above 100 keV. The IAM-AR results show the same overall behaviour as IAM-PCM, except that the cross section values are somewhat larger around the maximum, in seemingly excellent agreement with the measurements of Bolorizadeh and Rudd [49]. However, these cross section data have relatively large error bars. They were obtained from integrating absolute differential measurements and are deemed less accurate than those of reference [48], which were obtained from a more direct parallel-plate-capacitor method. Overall,

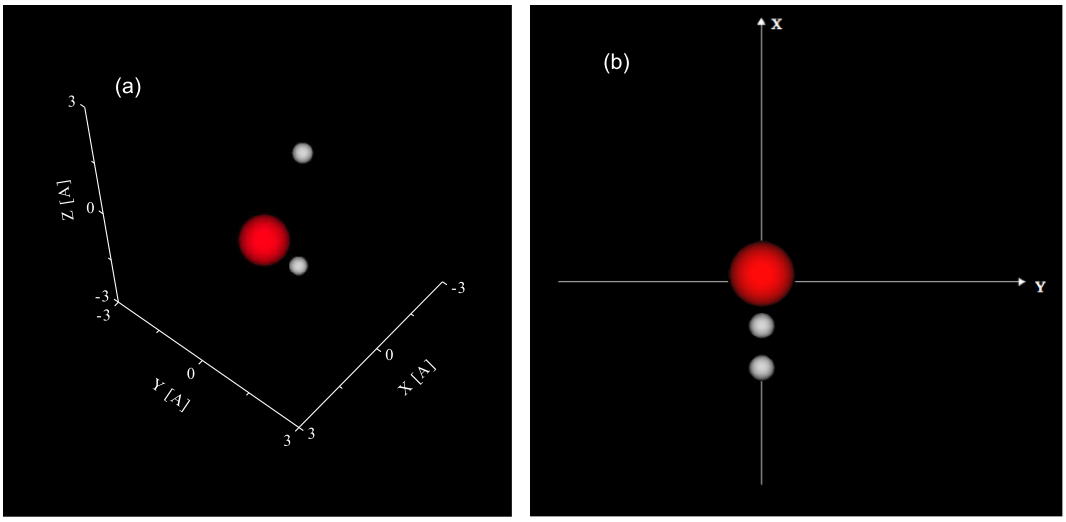

Fig. 3. Net capture in p-H_2O collisions at $E = 100$ keV: (a) three-dimensional image and (b) projection on the x–y plane. The radii of the spheres and circular disks are determined according to equation (25).

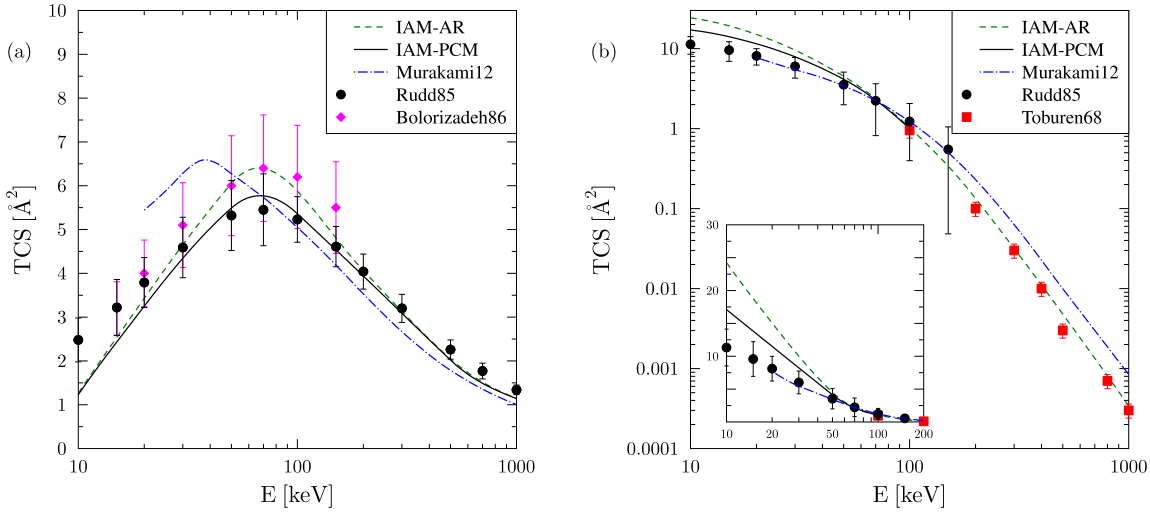

Fig. 4. Total cross sections for (a) net ionization and (b) net capture in p-H_2O collisions as functions of impact energy. Murakami12 refers to the molecular TC-BGM calculation of reference [23]. Experiments: Rudd85 [48], Bolorizadeh86 [49], Toburen68 [50].

the comparison indicates that the inclusion of geometric screening corrections via the IAM-PCM represents an improvement.

This becomes more obvious in the case of net capture. The linear plot in the inset of Figure 4b shows that the simple IAM-AR results in a strong overestimation towards low energies where the atomic capture cross sections are large (cf. Fig. 1). The overlap effect is significant (cf. Fig. 2) and leads to a substantial reduction of the molecular cross section. Still, the IAM-PCM results overestimate the experimental data at energies below 30 keV. It was argued in reference [35] that this overestimation is a consequence of the strong (resonant) p-H contributions in the IAM, which are unphysical given that there is no resonant capture channel in the p-H_2O collision system. The comparison with the molecular TC-BGM calculations confirms this. Down to the lowest energy of 20 keV for which these calculations were carried out they are in excellent agreement with the experimental data.

The situation is different at energies above 100 keV where the overlap effect in the IAM is negligible (cf. Fig. 3). IAM-PCM and IAM-AR results coincide and are in excellent agreement with the measurements of Toburen et al. [50]. The molecular TC-BGM cross section is higher by about a factor of two in this region. No explanation for this discrepancy has been found yet [51].

4 Results for proton-cluster collisions

Motivated by the goal to aid the microscopic understanding of proton cancer therapy a recent theoretical work looked into proton collisions from water clusters at $E = 100$ keV [52]. This is the region of the so-called Bragg

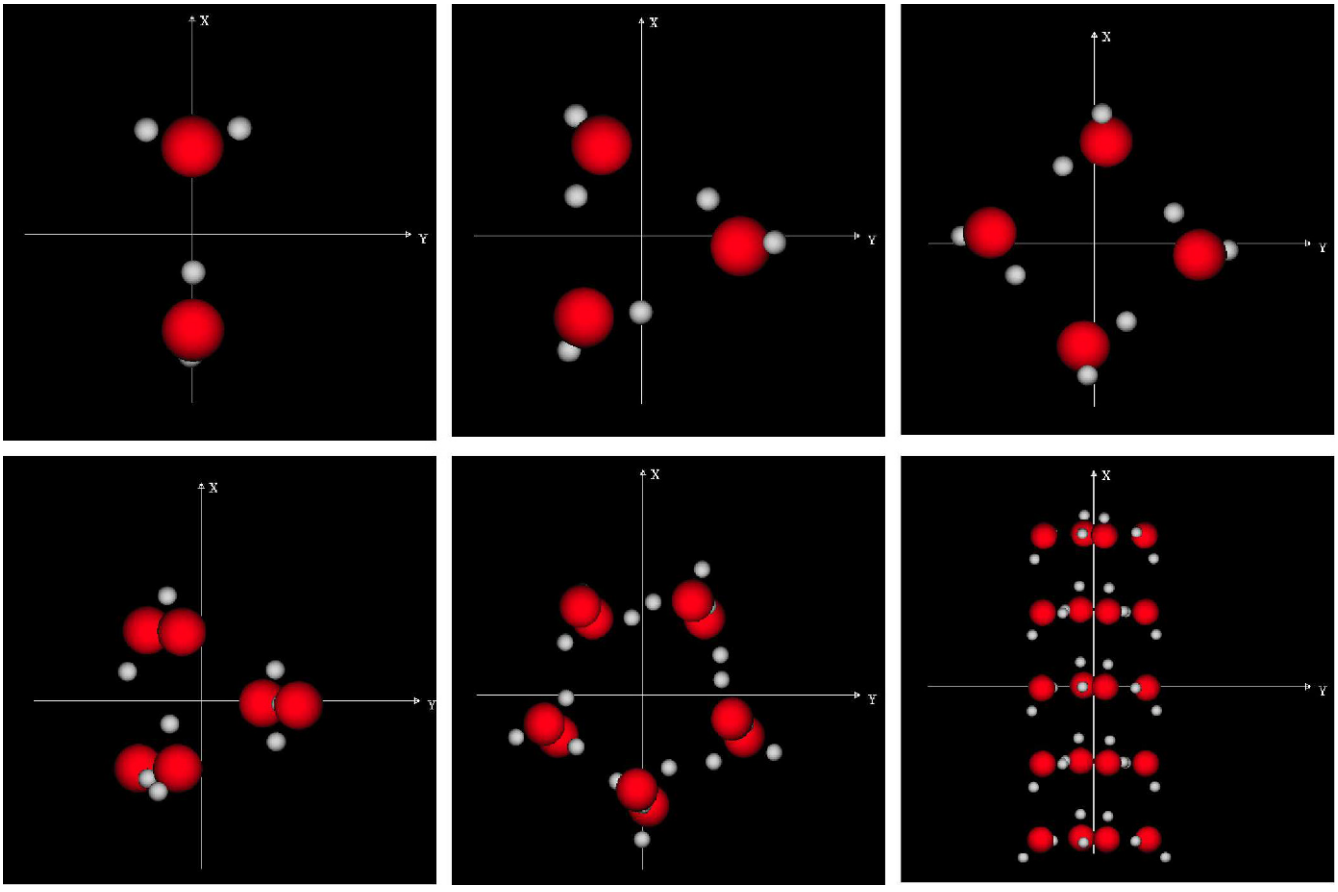

Fig. 5. Net capture cross sections in p-$(H_2O)_n$ collisions at $E = 100$ keV for $n = 2, 3, 4, 6, 10, 20$ from top left to bottom right. The representation is analogous to those of Figures 2b and 3b with radii determined acoording to equation (25). The corresponding plots of net ionization are similar, but show larger disks and more significant overlap, since the atomic ionization cross sections are larger.

peak, which marks the point of maximum energy deposition near the end of the path of an ion traveling through matter [53].

The calculation of reference [52] was based on the simplest-level electron nuclear dynamics (SLEND) method (see also Ref. [27]), in which classically moving nuclei are nonadiabatically coupled to electrons represented in terms of an unrestricted Hartree-Fock (UHF) determinantal wave function. Based on calculations for $(H_2O)_n$ with $n = 1, \ldots, 6$ it was found that the total (one-electron) capture cross section $\sigma(n)$ scaled as $n^{2/3}$. This was rationalized by associating each cluster with a sphere of volume $V(n)$, assuming $V(n) \propto n$ and arguing that the capture cross section should be proportional to the effective area of the sphere exposed to the incident ion. Ionization was not considered in reference [52], since the basis sets used did not allow for a representation of the continuum part of the spectrum. In addition, ETFs (cf. Eq. (8)) were neglected.

We have applied the IAM-PCM to test the prediction of reference [52] and to explore the scaling of both net capture and net ionization cross sections in p-$(H_2O)_n$ collisions in the impact energy range from 10 to 1000 keV and for cluster sizes up to $n = 20$. Specifically, we used the set of isomers included in the Cambridge Cluster Database [54][1], whose structures were calculated at the restricted Hartree-Fock/6-31G(d, p) level [55]. Figure 5 shows the IAM-PCM net capture cross sections at $E = 100$ keV for a subset of these clusters and arbitrary geometries in a similar representation as used in Figures 2b and 3b. As a consequence of the relatively large distances between the monomers in the clusters and the relative weakness of electron capture at 100 keV (cf. Fig. 4b) the overlap effect is small. This suggests the cross section scaling $\sigma^{\text{net cap}}(n) \propto n^{\alpha}$ with a value of α close to one. Indeed, as Figure 6 shows, the IAM-PCM capture results for $n = 1, \ldots, 20$ are almost perfectly fitted by

$$\sigma^{\text{net } x}(n) = an^{\alpha} \tag{28}$$

with $a = 1.0$ Å^2 and $\alpha = 0.97$. Here a represents an effective capture (or ionization) cross section (in Å^2) for the case $n = 1$, but is treated as a fit parameter in order not to give too much weight to the monomer.

Ionization is stronger than capture at $E = 100$ keV (cf. Fig. 4) and, accordingly, the overlap effect is larger.

[1] For $(H_2O)_6$ we chose the prism structure and omitted the cage structure.

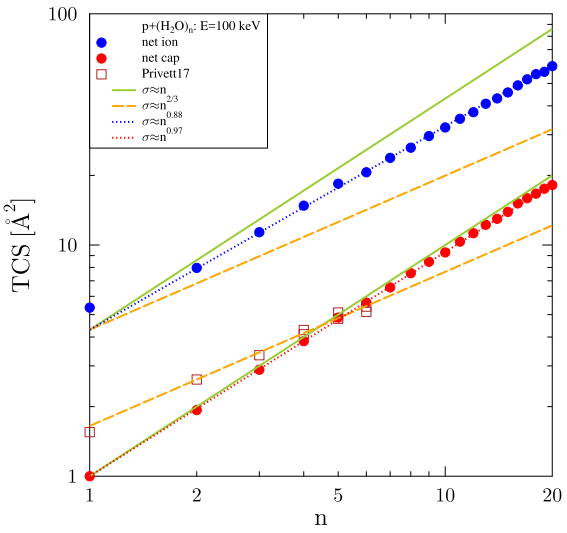

Fig. 6. Total cross sections for net ionization and net capture in p-$(H_2O)_n$ collisions at $E = 100$ keV as functions of cluster size n. The straight lines are obtained from equation (28) for different parameter choices and are included to guide the eye. Privett17: SLEND calculation for one-electron capture from reference [52].

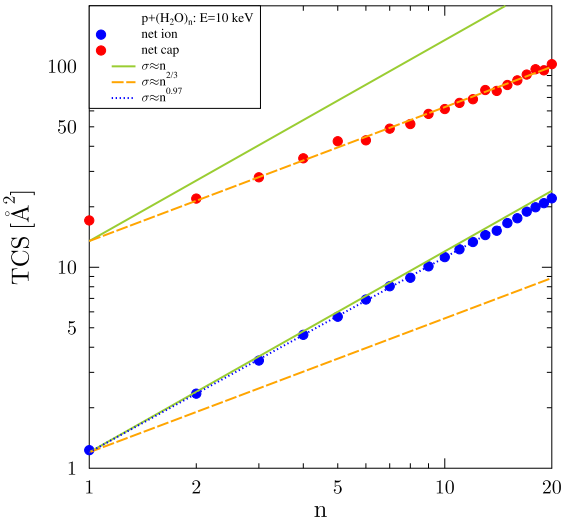

Fig. 7. Total cross sections for net ionization and net capture in p-$(H_2O)_n$ collisions at $E = 10$ keV as functions of cluster size n. The straight lines are obtained from equation (28) for different parameter choices and are included to guide the eye.

This translates into the optimal fit parameter $\alpha = 0.88$, which is still substantially larger than the value $\alpha = 0.67$ found by Privett et al. [52]. The different scaling behaviour between our calculations (which treat ionization properly) and those of reference [52] may have various reasons. Our calculations are based on a model, whereas Privett et al. considered the molecular structure of the water clusters in the UHF framework. As mentioned above, ETFs and ionization channels were neglected in their calculations. Also, they did not consider net capture, but one-electron capture. The latter is probably a minor concern given that both quantities should be similar in a calculation in which the only other contribution to net capture is two-electron capture.

Figure 7 shows IAM-PCM results for net capture and net ionization at $E = 10$ keV. For capture the overlap effect is large at low impact energy and the best fit of the calculations is obtained with $\alpha = 0.67$. By contrast, ionization is weak and $\sigma^{\text{net ion}}(n)$ scales almost linearly with n. Linear scaling is also obtained at high energies where the IAM-PCM cross sections for net ionization and net capture approach the IAM-AR predictions.

We tabulated the optimal parameters α and a for both net ionization and net capture at all impact energy values in the $10 \leq E \leq 1000$ keV range for which we carried out calculations and found that the IAM-PCM cross section results can be parametrized by using equation (28) and assuming

$$\alpha(a) = \begin{cases} -a/36.0 + 1.0 & \text{if } a \leq 12.0\,\text{Å}^2 \\ 2/3 & \text{otherwise} \end{cases} \qquad (29)$$

for the exponent. This is demonstrated in Figure 8. Each point on the graph corresponds to the best fit of the IAM-PCM $\sigma^{\text{net } x}(n)$ results for a given E to equation (28), i.e., to slope and intercept of that straight line that fits the cross section results for capture or ionization on a double-logarithmic plot as used in Figures 6 and 7 for $E = 100$ and $E = 10$ keV, respectively.

The only deviation from the almost perfect linear dependence of α on a is observed for net capture at the lowest energy $E = 10$ keV (i.e., the point at $a = 13.5$ Å^2), suggesting that α cannot fall below 0.67. This lower limit is implemented explicitly in the parametrization by the piecewise definition of $\alpha(a)$ and seems plausible given the arguments provided by Privett et al. [52] and the geometrical construction of the IAM-PCM cross section. In other words, the IAM-PCM appears to be consistent with those arguments in the limit of strong overlap. In the limit of weak overlap, the IAM-PCM approaches the IAM-AR prediction of a linear cross section scaling with cluster size n. Given the energy dependence of the atomic cross section magnitudes and overlaps the n-dependence is not universally determined by the geometry of the cluster as the arguments provided by Privett et al. might suggest.

To further test these observations we carried out IAM-PCM calculations for proton impact on neon clusters. The relevant structure information is also taken from the Cambridge Cluster Database using $d = 3.3$ a.u. as the internuclear distance of the dimer [54]. For p-Ne_n collisions with $n = 1, \ldots, 20$ we find $\alpha \geq 0.9$ for both net capture and net ionization in the entire impact energy range from 10 to 1000 keV. Figure 9 shows the IAM-PCM cross sections and the fits according to equation (28) at $E = 10$ keV. The cross sections are smaller than for p-$(H_2O)_n$ collisions, since the Ne electrons are more tightly bound. Given that the average distance between the monomers is similar in neon and water clusters, the atomic cross section overlaps are smaller and α is larger for the former.

Remarkably, the p-Ne_n results over the entire impact energy range can also be parametrized by equation (29).

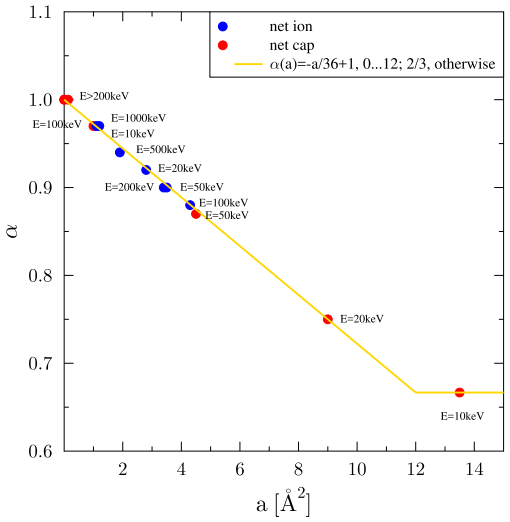

Fig. 8. The exponent α in equation (28) for net ionization and net capture in p-$(H_2O)_n$ collisions plotted versus the parameter a. Each data point corresponds to the best fit of the IAM-PCM results for $\sigma^{\mathrm{net}\,x}(n)$ by equation (28) at the indicated impact energy. The full line corresponds to the parametrization (29).

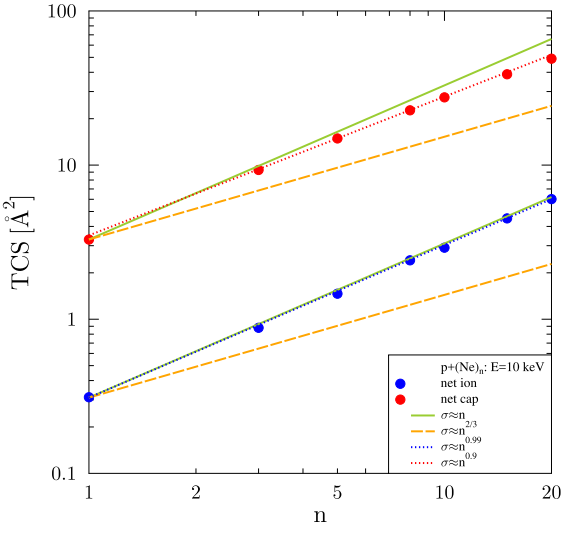

Fig. 9. Total cross sections for net ionization and net capture in p-Ne_n collisions at $E = 10$ keV as functions of cluster size n. The straight lines are obtained from equation (28) for different parameter choices and are included to guide the eye.

This is shown in Figure 10, which is analogous to Figure 8 for p-$(H_2O)_n$ collisions. The range of $\alpha(a)$ points for neon clusters is compressed compared to Figure 8 reflecting the smaller atomic cross sections and overlaps.

Finally, we consider proton collisions from a selection of carbon clusters C_n with $20 \leq n \leq 60$. The relevant structure information is taken from reference [56]. Similarly to the $(H_2O)_n$ case we find that net capture scales as $n^{2/3}$ at low energy, while α approaches unity more slowly than for water clusters towards higher energies. In the case of net ionization we also obtain somewhat smaller α values for C_n than for $(H_2O)_n$ signaling larger overlaps. Figure 11 illustrates these observations for $E = 100$ keV. For capture

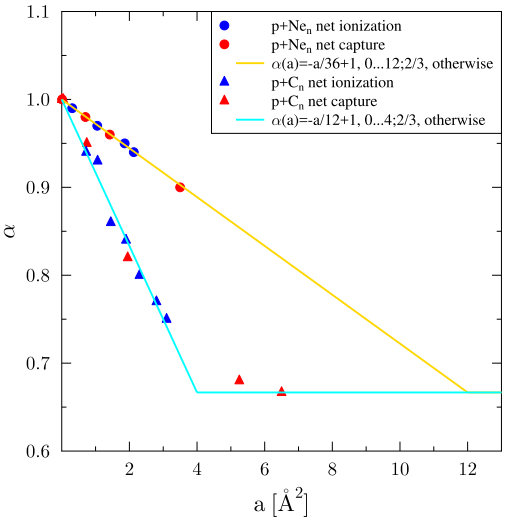

Fig. 10. The exponent α in equation (28) for net ionization and net capture in p-Ne_n and p-C_n collisions plotted versus the parameter a. Each data point corresponds to the best fit of the IAM-PCM results for $\sigma^{\mathrm{net}\,x}(n)$ by equation (28) at a given impact energy. The yellow line corresponds to the parametrization (29) and the light-blue line to (30).

the optimal α value is 0.95, while for ionization $\alpha = 0.77$ provides the best fit of the IAM-PCM calculations. This is to be contrasted with $\alpha = 0.97$ and $\alpha = 0.88$ for p-$(H_2O)_n$ collisions, respectively (cf. Figure 6).

The parametrization (29) does not work for fullerenes, but we found that the ansatz (28) together with

$$\alpha(a) = \begin{cases} -a/12.0 + 1.0 & \text{if } a \leq 4.0\,\text{Å}^2 \\ 2/3 & \text{otherwise} \end{cases} \qquad (30)$$

provides a good fit of the results in the 10 to 1000 keV impact energy range. These results are included in Figure 10. One may argue that the slope of $\alpha(a)$ for a given cluster species is reflective of the average distance between monomers in the clusters. Additional calculations for p-Ar_n support this and all data taken together suggest that the slope is approximately inversely proportional to that distance. Systematic measurements for a set of clusters over a range of impact energies would be highly desirable to test these predictions.

Experimental data are available for net ionization of C_{60} at high impact energies [57]. In Figure 12 we compare these measurements with IAM-PCM and IAM-AR calculations. The overlap effect is significant, reducing the net ionization cross section by more than a factor of two for most of the impact energy interval shown. The experimental data are even lower than the IAM-PCM results with the latter just lying outside of the error bars. One can regard the agreement as fair. Clearly, data at lower energies (and for net capture as well) would be needed for a better assessment of the quality of the IAM-PCM results.

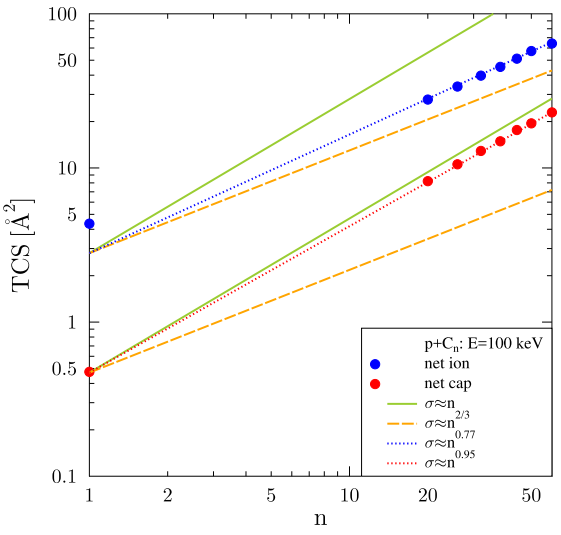

Fig. 11. Total cross sections for net ionization and net capture in p-C_n collisions at $E = 100$ keV as functions of cluster size n. The straight lines are obtained from equation (28) for different parameter choices and are included to guide the eye.

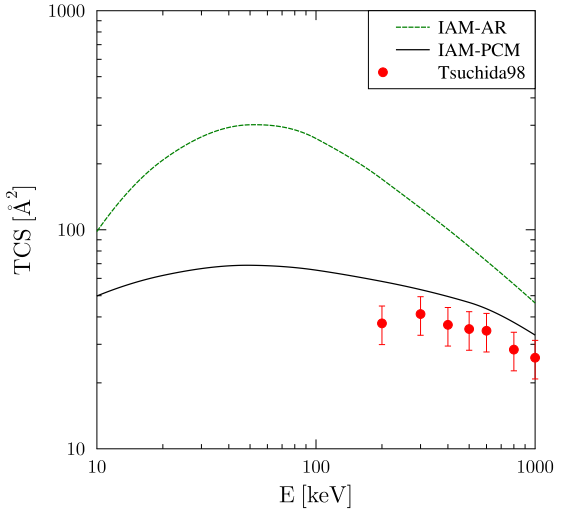

Fig. 12. Total cross section for net ionization in p-C_{60} collisions as function of impact energy. Experimental data: Tsuchida98 [57].

5 Concluding remarks

34 years after the publication of the Runge-Gross theorem full-fledged TDDFT calculations for ion-impact collisions have remained a rarity compared to the widespread application of TDDFT to laser-matter interaction problems. As yet, simplified approaches and models are indispensable for a semi-quantitative understanding of electron removal processes in collisions involving complex multicenter Coulomb systems. The IAM-PCM is one such model. It is based on a geometrical interpretation of the cross section as an effective area composed of overlapping circular disks whose areas represent the atomic cross sections that contribute to net capture or net ionization in the system of interest. The atomic cross sections are calculated based on a TDDFT-inspired single-particle description using atomic ground-state DFT potentials and the two-center basis generator method for orbital propagation. The effective area calculation is carried out using a pixel counting method.

The IAM-PCM is flexible and efficient. Once the atomic cross sections have been calculated and the required information on the geometric structure of the target, i.e., the equilibrium positions of the nuclei, is available it takes about three minutes on a single-core desktop or laptop computer to calculate the net ionization or net capture cross section at a given impact energy for a system as complex as C_{60}.

To date, we have applied the IAM-PCM to proton collisions from a variety of targets: covalently bound molecules in reference [39] and, in this work, clusters with hydrogen bonds ($(H2O)_n$), van der Waals clusters (Ne_n), and covalently-bound fullerenes (C_n). One major objective of this work has been to test and generalize a scaling law found by Privett et al. [52] in capture from water clusters at $E = 100$ keV to capture and ionization over a wide range of energies.

Our results can be summarized as follows: both net capture and net ionization cross sections at a given impact energy scale as n^α, but α varies as a function of E and reaches the value of 2/3 found by Privett et al. for one-electron capture only in situations in which the atomic cross section overlaps are large. This is the case for capture at low impact energy ($E = 10$ keV) in p-$(H2O)_n$ and p-C_n collisions, but not in p-Ne_n collisions and never for ionization. For capture from water clusters at $E = 100$ keV we find $\alpha = 0.97$ in stark contrast to the result of Privett et al.

Furthermore, we showed that the variations of α can be modeled by the ansatz $\sigma^{\mathrm{net}\,x} = an^{\alpha(a)}$ and a linear functional dependence of α on a. Our results suggest that the slope of this linear function is largely determined by the average distance between the monomers in a given cluster. It will be interesting to see how general this result is and where its limitations are. Further calculations for other systems and, more importantly, systematic experimental measurements will be required to answer this question.

This work was supported by the Natural Sciences and Engineering Research Council of Canada (NSERC). One of us (H.J.L.) would like to thank the Center for Scientific Computing, University of Frankfurt for making their High Performance Computing facilities available.

Author contribution statement

All the authors were involved in the preparation of the manuscript. All the authors have read and approved the final manuscript.

References

1. I.K. Gainullin, M.A. Sonkin, Comput. Phys. Commun. **188**, 68 (2015)
2. E. Runge, E.K.U. Gross, Phys. Rev. Lett. **52**, 997 (1984)

3. M.A.L. Marques, E.K.U. Gross, Annu. Rev. Phys. Chem. **55**, 427 (2004)
4. M.A.L. Marques, N.T. Maitra, F.M.S. Nogueira, E.K.U. Gross, A. Rubio (Eds.) in *Fundamentals of time-dependent density functional theory*, Lecture notes in physics (Springer, Berlin, 2012), Vol. 837
5. C.A. Ullrich, *Time-dependent density-functional theory: concepts and applications* (Oxford University Press, Oxford, 2012)
6. W. Fritsch, C.D. Lin, Phys. Rep. **202**, 1 (1991)
7. B.H. Bransden M.R.C. McDowell, *Charge exchange and the theory of ion-atom collisions* (Clarendon Press, Oxford, 1992)
8. M. Baxter, T. Kirchner, Phys. Rev. A **93**, 012502 (2016)
9. K.C. Kulander, K.R. Sandhya Devi, S.E. Koonin, Phys. Rev. A **25**, 2968 (1982)
10. W. Stich, H.J. Lüdde, R.M. Dreizler, Phys. Lett. **41**, 99A (1983)
11. K. Gramlich, N. Grün, W. Scheid, J. Phys. B **19**, 1457 (1986)
12. J.J. Griffin, P.C. Lichtner, M. Dworzecka, Phys. Rev. C **21**, 1351 (1980)
13. Y. Alhassid, S.E. Koonin, Phys. Rev. C **23**, 1590 (1981)
14. T. Kirchner, L. Gulyás, H.J. Lüdde, A. Henne, E. Engel, R.M. Dreizler, Phys. Rev. Lett. **79**, 1658 (1997)
15. T. Kirchner, L. Gulyás, H.J. Lüdde, E. Engel, R.M. Dreizler, Phys. Rev. A **58**, 2063 (1998)
16. O.J. Kroneisen, H.J. Lüdde, T. Kirchner, R.M. Dreizler, J. Phys. A **32**, 2141 (1999)
17. M. Zapukhlyak, T. Kirchner, H.J. Lüdde, S. Knoop, R. Morgenstern, R. Hoekstra, J. Phys. B **38**, 2353 (2005)
18. T. Kirchner, H.J. Lüdde, M. Horbatsch, Recent Res. Dev. Phys. **5**, 433 (2004)
19. A.C.K. Leung, T. Kirchner, Phys. Rev. A **4**, 042703 (2017)
20. T. Kirchner, M. Horbatsch, H.J. Lüdde, R.M. Dreizler, Phys. Rev. A **62**, 042704 (2000)
21. K.C. Kulander, Phys. Rev. A **38**, 778 (1988)
22. H.J. Lüdde, T. Spranger, M. Horbatsch, T. Kirchner, Phys. Rev. A **80**, 060702(R) (2009)
23. M. Murakami, T. Kirchner, M. Horbatsch, H.J. Lüdde, Phys. Rev. A **85**, 052704 (2012)
24. A. Salehzadeh, T. Kirchner, Eur. Phys. J. D **71**, 66 (2017)
25. X. Hong, F. Wang, Y. Wu, B. Gou, J. Wang, Phys. Rev. A **93**, 062706 (2016)
26. E.E. Quashie, B.C. Saha, X. Andrade, A.A. Correa, Phys. Rev. A **95**, 042517 (2017)
27. A.J. Privett, J.A. Morales, Chem. Phys. Lett **603**, 82 (2014)
28. M.C. Bacchus-Montabonel, Chem. Phys. Lett. **664**, 173 (2016)
29. C. Covington, K. Hartig, A. Russakoff, R. Kulpins, K. Varga, Phys. Rev. A **95**, 052701 (2017)
30. C. Dal Cappello, P.A. Hervieux, I. Charpentier, F. Ruiz-Lopez, Phys. Rev. A **78**, 042702 (2008)
31. H. Lekadir, I. Abbas, C. Champion, O. Fojón, R.D. Rivarola, J. Hanssen, Phys. Rev. A **79**, 062710 (2009)
32. C. Champion, P.F. Weck, H. Lekadir, M.E. Galassi, O.A. Fojón, P. Abufager, R.D. Rivarola, J. Hanssen, Phys. Med. Biol. **57**, 3039 (2012)
33. P. de Vera, R. Garcia-Molina, I. Abril, A.V. Solov'yov, Phys. Rev. Lett. **110**, 148104 (2013)
34. L. Sarkadi, Phys. Rev. A **92**, 062704 (2015)
35. H.J. Lüdde, A. Achenbach, T. Kalkbrenner, H.-C. Jankowiak, T. Kirchner, Eur. Phys. J. D **70**, 82 (2016)
36. R. van Leeuwen, Phys. Rev. Lett. **82**, 3863 (1999)
37. J.D. Talman, W.F. Shadwick, Phys. Rev. A **14**, 36 (1976)
38. E. Engel, S.H. Vosko, Phys. Rev. A **47**, 2800 (1993)
39. H.J. Lüdde, A. Henne, T. Kirchner, R.M. Dreizler, J. Phys. B **29**, 4423 (1996)
40. A.C. Hindmarsh, ODEPACK, A Systematized Collection of ODE Solvers, in *Scientific computing*, edited by R. Stepleman (Elsevier, North-Holland, Amsterdam, 1983), pp. 55–64
41. H.J. Lüdde, in *Many-particle quantum dynamics in atomic and molecular fragmentation*, edited by J. Ullrich, V.P. Shevelko (Springer, Heidelberg, 2003), p. 205
42. H. Bethe, Ann. Phys. **5**, 325 (1930)
43. M. Inokuti, Rev. Mod. Phys. **43**, 297 (1971)
44. I.B. Abdurakhmanov, A.S. Kadyrov, S.K. Avazbaev, I. Bray, J. Phys. B **49**, 115203 (2016)
45. T. Kirchner, H.J. Lüdde, M. Horbatsch, R.M. Dreizler, Phys. Rev. A **61**, 052710 (2000)
46. T. Kirchner, H.J. Lüdde, R.M. Dreizler. Phys. Rev. A **61**, 012705 (2000)
47. F. Blanco, G. García, Phys. Lett. A **317**, 458 (2003)
48. M.E. Rudd, T.V. Goffe, R.D. DuBois, L.H. Toburen, Phys. Rev. A **31**, 492 (1985)
49. M.A. Bolorizadeh, M.E. Rudd, Phys. Rev. A **33**, 888 (1986)
50. L.H. Toburen, M.Y. Nakai, R.A. Langley, Phys. Rev. **171**, 114 (1968)
51. T. Kirchner, M. Murakami, M. Horbatsch, H.J. Lüdde, Adv. Quant. Chem. **65**, 315 (2013)
52. A.J. Privett, E.S. Teixeira, C. Stopera, J.A. Morales, PLoS ONE **12**, e0174456 (2017)
53. H. Bichsel, Adv. Quant. Chem. **65**, 1 (2013)
54. D.J. Wales, J.P.K. Doye, A. Dullweber, M.P. Hodges, F.Y. Naumkin, F. Calvo, J. Hernández-Rojas, T.F. Middleton, The Cambridge Cluster Database. Available at http://www-wales.ch.cam.ac.uk/CCD.html [Online; accessed 2018-02-23]
55. S. Maheshwary, N. Patel, N. Sathyamurthy, A.D. Kulkarni, S.R. Gadre, J. Phys. Chem. A **105**, 10525 (2001)
56. Michigan State University Computational Nanotechnology Lab. Available at http://www.nanotube.msu.edu/fullerene/fullerene-isomers.html [Online; accessed 2018-02-22]
57. H. Tsuchida, A. Itoh, Y. Nakai, K. Miyabe, N. Imanishi, J. Phys. B **31**, 5383 (1998)
58. M.B. Shah, H.B. Gilbody, J. Phys. B **14**, 2361 (1981)
59. M.B. Shah, D.S. Elliott, H.B. Gilbody, J. Phys. B **20**, 2481 (1987)
60. M.E. Rudd, Y.K. Kim, D.H. Madison, J.W. Gallagher, Rev. Mod. Phys. **57**, 965 (1985)
61. G.W. McClure, Phys. Rev. **148**, 47 (1966)
62. J.E. Bayfield. Phys. Rev. **185**, 105 (1969)
63. A.B. Wittkower, G. Ryding, H.B. Gilbody, Proc. Phys. Soc. **89**, 541 (1966)
64. M.E. Rudd, R.D. DuBois, L.H. Toburen, C.A. Ratcliffe, T.V. Goffe, Phys. Rev. A **28**, 3244 (1983)